Chapter 4

Simulation results for magnetized plasmas

In this chapter, we consider the dust charge fluctuation mode and lower hybrid wave damping in a magnetized plasma. Also, we consider plasma instabilities associated with streaming of dust relative to the background plasma across a magnetic field as well as the expansion of a dust cloud into a background plasma across a magnetic field. Results from the linearized versions of the model equations are utilized to guide the simulation results. The linearized quantities for the plasma and dust are taken to be

$$\begin{aligned} n_{\mathrm{e,i}} &= n_{\mathrm{e0,i0}} + \tilde{n}_{\mathrm{e,i}}, \\ \vec{v}_{\mathrm{e,i}} &= \vec{v}_{\mathrm{e0,i0}} + \tilde{\vec{v}}_{\mathrm{e,i}}, \\ n_{\mathrm{d}} &= n_{\mathrm{d0}} + \tilde{n}_{\mathrm{d}}, \\ Q_{\mathrm{d}} &= Q_{\mathrm{d0}} + \tilde{Q}_{\mathrm{d}}, \\ I_{\mathrm{e,i}} &= I_{\mathrm{e0,i0}} + \tilde{I}_{\mathrm{e,i}}, \\ \phi_{\mathrm{f}} &= \phi_{\mathrm{f0}} + \tilde{\phi}_{\mathrm{f}}, \end{aligned}$$

where the zeroth and first order terms are denoted. The first order terms are taken to have $\exp(i\vec{k}\cdot\vec{x} - i\omega t)$ spatial and temporal dependence. All numerical simulations are initialized charge neutral with the number of positive and negative charges equal, that is, $en_{\mathrm{e0}} + Q_{\mathrm{d0}}n_{\mathrm{d0}} = en_{\mathrm{i0}}$. All dust grains are initialized with $I_{\mathrm{e0}} + I_{\mathrm{i0}} = 0$ in the absence of perturbations as described in section 3.6. The simulation box used is 128×128 or 256×128 grid cells. The theory and the details of simulation results are presented in

the following sections.

4.1 Dust Charge Fluctuation Mode

4.1.1 Theory

Our first investigation is a fundamental study of the dust charge fluctuation mode. This is a fundamental wave mode in dusty plasmas that results from dust charging. It has been described theoreticaly by other investigators [*Jana et al.*, 1993; *Jana et al.*, 1995; *Varma et al.*, 1993]. Using equation (3.8), the dust charge fluctuations due to the plasma current fluctuations can be expressed by

$$\frac{d\tilde{Q}_{\mathrm{d}}}{dt} = \tilde{I}_{\mathrm{e}} + \tilde{I}_{\mathrm{i}}. \tag{4.1}$$

Linearizing the currents, equation (3.11) and (3.12), the dust charge fluctuation dynamics equation can be shown to be [*Jana et al.*, 1993]

$$\frac{d\tilde{Q}_{\mathrm{d}}}{dt} + \eta\tilde{Q}_{\mathrm{d}} = |I_{e0}| \left(\frac{\tilde{n}_{\mathrm{i}}}{n_{\mathrm{i}0}} - \frac{\tilde{n}_{\mathrm{e}}}{n_{\mathrm{e}0}} \right), \tag{4.2}$$

where the dust charge fluctuation relaxation rate η is given by

$$\eta = \frac{e|I_{\mathrm{e}0}|}{C} \left(\frac{1}{kT_{\mathrm{e}}} + \frac{1}{kT_{\mathrm{i}} - e\phi_{\mathrm{f}0}} \right). \tag{4.3}$$

Physically η describes the rate at which a perturbation to the dust charge will decay back to the equilibrium value. Equation (4.2) shows that dust charge fluctuations may be driven by electron and ion density perturbations ($\tilde{n}_{\rm e}$, $\tilde{n}_{\rm i}$) such as those produced by plasma waves. The dust charge fluctuations damp in the absence of electron and ion density perturbations. The damped mode is described as [*Jana et al.*, 1993; *Varma et al.*, 1993]

$$\omega \approx -i\eta. \tag{4.4}$$

To investigate this mode, we initialize the dust charge with a 10% perturbation given by

$$Q_{\rm d}(x, y, t = 0) = Q_{\rm d0}(1 + 0.1\cos(k_{\rm x}x)) \tag{4.5}$$

where $k_{\rm x} = \frac{2\pi m}{L}$ (m = 5 for mode 5 in our study) and $Q_{\rm d0} = 1000$ electrons. The dust density is 100 particles per cell, the dust charge density is 1% of the ion charge density, and $\tilde{n}_{\rm e} = \tilde{n}_{\rm i} = \tilde{n}_{\rm d} = 0$.

4.1.2 Results

Figure 4.1 (a) shows the dust charge temporal decay for a single dust particle. The dust particle is arbitrarily chosen to have the maximum positive charge perturbation at $t = 0$, that is, $\tilde{Q}_{\rm d} = +\ 0.1Q_{\rm d0}$. Three values of the normalized dust fluctuation relaxation constant $\tilde{\eta} = \eta/\omega_{\rm lh}$, 0.05, 0.25, and 0.5, are shown. It can be seen that the e-folding decay of the dust charge agrees well with the prediction of (4.4). Figure 4.1 (b) shows the decay of the dust charge perturbation in the simulation box for the fixed value of $y/\Delta y = 64$ and $\tilde{\eta} = 0.05$.

Figure 4.2 shows the current temporal decay of a single dust particle for $\tilde{\eta} = 0.05$, 0.25, and 0.50. Again the dust grain is arbitrary chosen to have the maximum positive perturbation $\tilde{Q}_{\rm d} = +\,0.1Q_{\rm d0}$. For this positive charge perturbation, the corresponding electron current perturbation is negative and the ion perturbation is positive as can be seen in Figure 4.2. For the case $\tilde{\eta} = 0.5$, it can be seen that on the time scale of η^{-1}, the electron and ion currents approach the equilibrium value I_0 where $I_0 = |I_{\rm e0}| = |I_{\rm i0}|$. This brings the dust grain charge and potential back to the equilibrium values $Q_{\rm d0}$ and $\phi_{\rm f0}$ since

$$I_{\rm e} + I_{\rm i} \rightarrow 0. \tag{4.6}$$

For higher values of $\tilde{\eta} = 0.25$ and 0.5, it can be seen that the currents reach equilibrium faster as expected. Note that the slow decrease in the equilibrium current as time evolves is due to the slow reduction in the background plasma density from the dust charging since the production rate $q_{\rm s} = 0$ for these results. Figure 4.3 shows the electron and ion current and density at $\omega_{\rm lh}t = 0$, 30, and 60 for $y/\Delta y = 64$. The electron and ion current perturbed with (4.5) are 180^o out of phase. The small electron and ion density in-phase perturbation result from the decay of the dust charge fluctuation.

4.2 Damping of Lower Hybrid Oscillations due to Dust Charging

4.2.1 Theory

Damping of plasma waves in a dusty plasmas due to dust charging has been studied theoretically by several investigators [*Jana et al.*, 1993; *Jana et al.*, 1995; *Varma et al.*, 1993]. This collisionless damping is unique to dusty plasmas and our numerical model

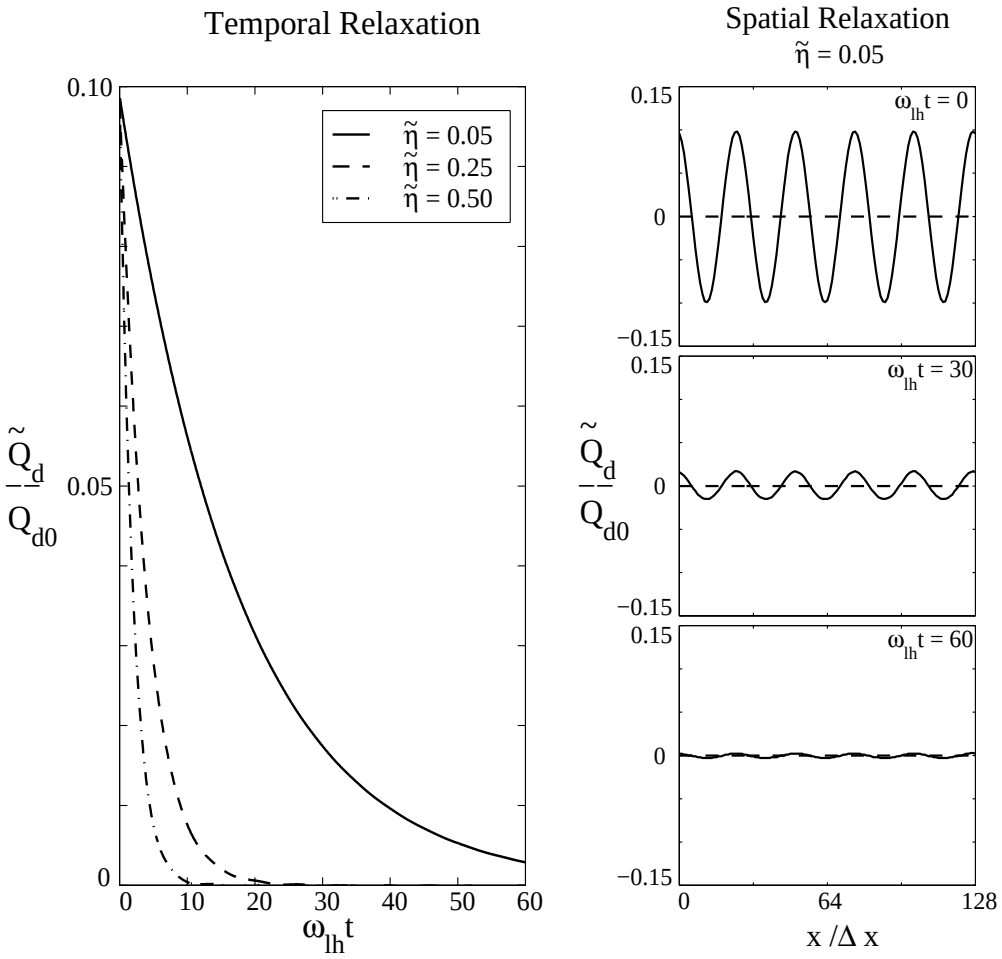

Figure 4.1: a. Dust charge fluctuation temporal decay for a specific dust particle. b. Spatial dust charge fluctuation decay for $\tilde{\eta}$=0.05.

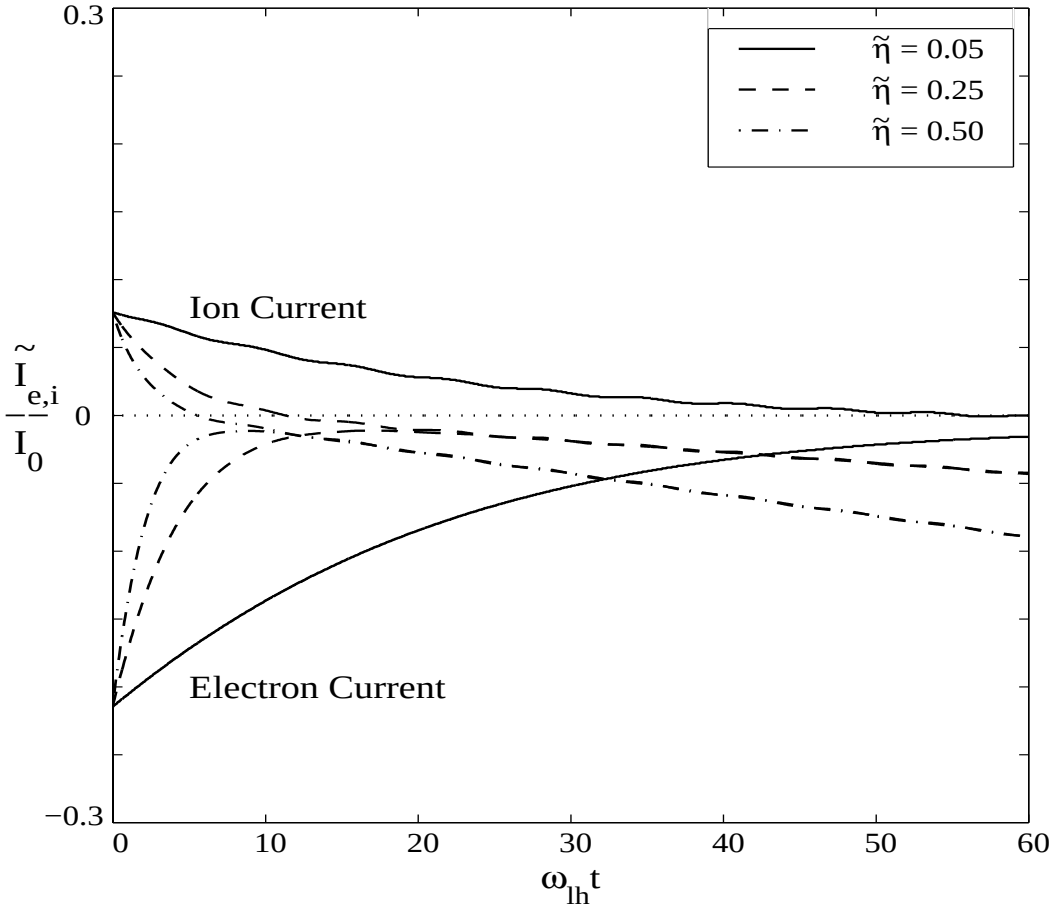

Figure 4.2: Current temporal decay for a specific dust particle for $\tilde{\eta}$=0.05, $\tilde{\eta}$=0.25, and $\tilde{\eta}$=0.50.

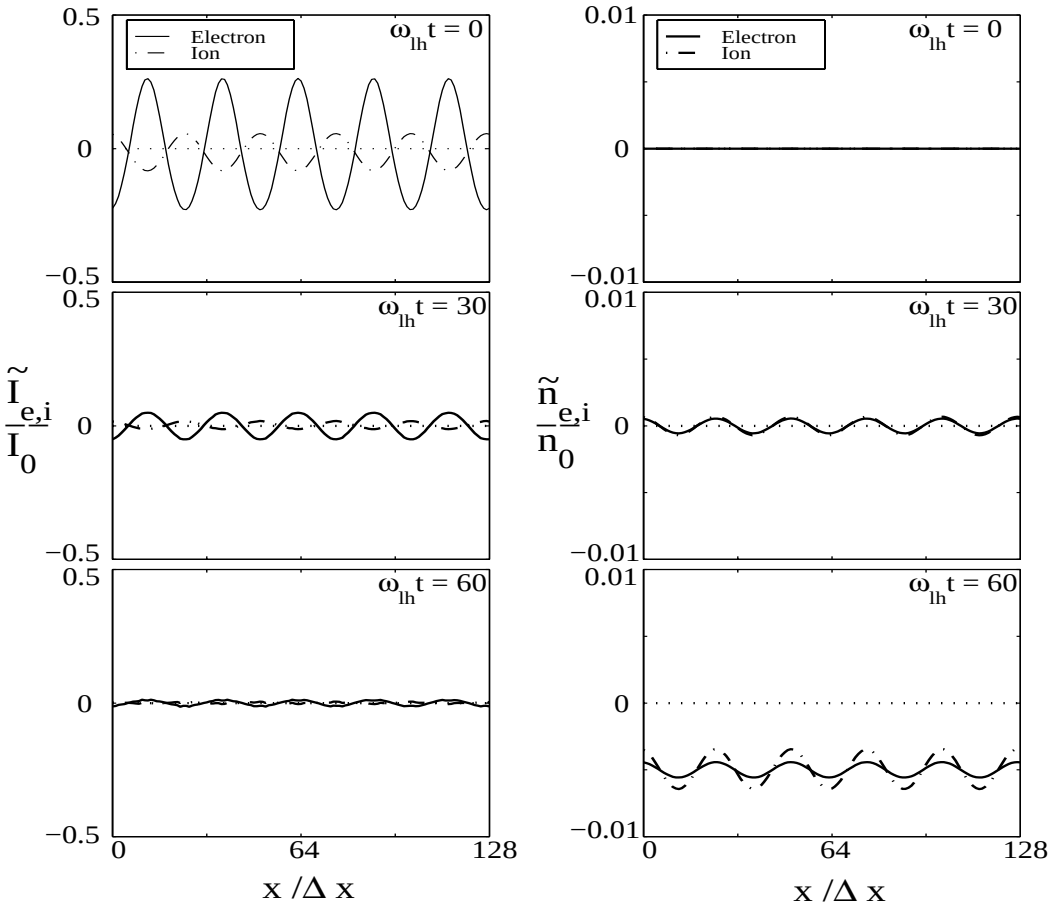

Figure 4.3: Spatial current temporal decay and density for $\tilde{\eta}$=0.05.

can provide insight into this fundamental process. The primary low frequency ion wave in our model is the lower hybrid wave. Our investigation here considers the damping of this wave mode by dust charging and the associated physical processes. To incorporate the effects of dust charge fluctuations into the dispersion relation for lower hybrid waves, we use the formalism described by other investigators. The general dispersion relation for electrostatic waves including the effects of dust charge fluctuations is given by [*Jana et al.*, 1993]

$$1 + \chi_{\mathrm{e}}(\omega, k)\left(1 + \frac{i\beta}{\omega + i\eta}\right) + \chi_{\mathrm{i}}(\omega, k)\left(1 + \frac{i\beta}{\omega + i\eta}\frac{n_{\mathrm{e0}}}{n_{\mathrm{i0}}}\right) + \chi_{\mathrm{d}}(\omega, k) = 0 \tag{4.7}$$

where $\chi_{\mathrm{e}}(\omega, k)$, $\chi_{\mathrm{i}}(\omega, k)$ and $\chi_{\mathrm{d}}(\omega, k)$ are the electron, ion, and dust susceptibilities, respectively. Note that to simplify our investigation here, we neglect the effects of the dust dynamics and take $\chi_{\mathrm{d}} = 0$ in (4.7). In general for lower hybrid waves, $\chi_{\mathrm{e}} = \omega_{\mathrm{pe}}^2/\Omega_{\mathrm{ce}}^2$ and $\chi_{\mathrm{i}} = -\omega_{\mathrm{pi}}^2/\omega^2$ where Ω_{ce} is the electron cyclotron frequency. It should be noted that in our model for strongly magnetized electrons, $\chi_{\mathrm{e}} = \omega_{\mathrm{pe}}^2/\Omega_{\mathrm{ce}}^2 \to 0$. Using these susceptibilities we can obtain the following dispersion relation

$$(\omega^2 - \omega_{\mathrm{lh}}^2)(\omega + i\eta) = -i\beta\frac{n_{\mathrm{e0}}}{n_{\mathrm{i0}}}\omega_{\mathrm{lh}}^2, \tag{4.8}$$

where in our strongly magnetized limit, the lower hybrid frequency $\omega_{\mathrm{lh}} = \omega_{\mathrm{pi}}$. The dispersion relation has been written in a form to make the wave modes it describes apparent. On the l.h.s of equation (4.8), the three roots correspond to the two lower hybrid modes and the dust charge fluctuation mode which was described in the previous section. The r.h.s describes the coupling of the lower hybrid modes to dust charge

fluctuations. The parameter β is the dust charge damping rate and is given by

$$\beta = \frac{|I_{e0}|}{e}\frac{n_{d0}}{n_{e0}}, \tag{4.9}$$

where n_{d0} is the equilibrium dust density and e is the unit charge. Typically, β describes the damping of a wave mode due to the dust charging. Solving this dispersion relation analytically under the assumption $\beta/\omega_{lh} < \eta/\omega_{lh} \ll 1$ gives the roots for the lower hybrid modes as

$$\omega \approx \pm\omega_{lh} - i\frac{\beta}{2}\frac{n_{e0}}{n_{i0}}. \tag{4.10}$$

Therefore, the damping rate $\nu = \frac{\beta}{2}\frac{n_{e0}}{n_{i0}}$ depends directly on the parameter β which may be interpreted as an effective collision frequency of electrons with the dust grains. Figure 4.4 shows the lower hybrid oscillation damping rate $\tilde{\nu} = \nu/\omega_{lh}$ for $\tilde{\eta} = 0.01$, 0.1, 0.5, and 1.0 with $n_{e0}/n_{i0} = 0.99$. In case of small $\tilde{\eta}$, the damping rate $\tilde{\nu}$ is propotional to $\tilde{\beta}/2$ as described in (4.10). As $\tilde{\eta}$ increases, the damping rate decreases and scales as $\tilde{\beta}/4$ for $\tilde{\eta} \approx 1.0$. From section 4.1, large $\tilde{\eta}$ is expected to inhibit the growth of dust fluctuations which in turn results in less damping of the ion waves as will be described shortly.

To study the damping of lower hybrid waves, we initialize the simulation with a weak 1% ion density perturbation of the form

$$n_i(x, y, t = 0) = n_{i0}(1 + 0.01\cos(k_x x)) \tag{4.11}$$

where $k_x = \frac{2\pi m}{L}$ and $m = 1$ for mode 1 used here. Also, we chose $\tilde{n}_e = \tilde{n}_d = \tilde{Q}_d = 0$ initially. In this case, we use 9 simulation dust particles per cell with an equilibrium dust charge $Q_{d0} = 1100$ electrons which gives a dust charge density of 1% of the background equilibrium ion charge density for the chosen value of n_{i0}.

4.2.2 Results

Figure 4.5 shows the potential and ion density for the lower hybrid mode for two cases, $\tilde{\beta} = \beta/\omega_{lh} = 0.00$ and 0.003. These cases correspond to $\tilde{\eta} = \eta/\omega_{lh} = 0.0$ and 1.0. The simulation is run for 100 initial lower hybrid periods. It can be seen that for the case $\tilde{\beta} = 0.003$, the lower hybrid mode is damped and the calculated damping rate is 0.0008 which agrees well with the theoretical estimation in Figure 4.4 of 0.00074. The decrease in frequency of the lower hybrid wave near the end of the simulation is due to the slow decrease in background plasma density due to the dust charging since the production rate $q_s = 0$ for these simulations. Also in Figure 4.5, it is seen that growth of dust charge fluctuations is associated with the damping of the lower hybrid mode. Therefore, it can be seen that the parameter $\tilde{\beta}$ provides a description of the response of dust fluctuations to electron and ion density perturbations and indicates a growth time for the dust fluctuations. Figure 4.6 shows a temporal plot of the ion density and dust charge for one lower hybrid period. It can be seen that the dust charge fluctuation lags the ion density by 135^o as is predicted by equation (4.2). Of course, the actual value of the phase lag depends on $\tilde{\eta}$ and this phase lag will be between 90^o (small $\tilde{\eta}$) and 180^o (large $\tilde{\eta}$).

4.3 Plasma Instability Associated with Streaming Dust

4.3.1 Theory

Streaming of dust relative to a background plasma across a magnetic field at velocities larger than the ion thermal velocity may provide free energy for the production of lower hybrid waves [*Rosenberg et al.*, 1999]. This lower hybrid streaming LHS instability may have important applications in space plasmas. For example, the LHS instability may produce irregularities in the ionospheric plasma that have been proposed to produce radar signal returns from the space shuttle exhaust [*Rosenberg et al.*, 1999; *Bernhardt et al.*, 1995]. Equation (4.7) may be used to study the linear dispersion relation of this instability. The electron and ion susceptibilities of the previous section may be used. In this case, the dust susceptibility $\chi_{\rm d} = -\omega_{\rm pd}^2/(\omega - kv_{\rm d})^2$ must be included where $\omega_{\rm pd}$ and $v_{\rm d}$ are the dust plasma frequency and streaming velocity, respectively. Using these susceptibilities in (4.7) and presently neglecting the effects of the dust charge fluctuations, the dispersion relation can easily be shown to be

$$\tilde{\omega}^4 \; - \; 2\tilde{k}\tilde{\omega}^3 \; + \; (\tilde{k}^2 - 1 - \tilde{\omega}_{\rm pd}^2)\tilde{\omega}^2 \; + \; 2\tilde{k}\tilde{\omega} \; - \; \tilde{k}^2 \; = \; 0 \tag{4.12}$$

where $\tilde{\omega} = \omega/\omega_{\rm lh}$, $\tilde{k} = kv_{\rm d}/\omega_{\rm lh}$, and $\tilde{\omega}_{\rm pd} = \omega_{\rm pd}/\omega_{\rm lh}$. Again note that for our strongly magnetized electron case, $\omega_{\rm lh} = \omega_{\rm pi}$. In our investigation here we will consider the classical weak cold beam limit for simplicity. In this case, the growth rate γ is given by [*Rosenberg et al.*, 1999]

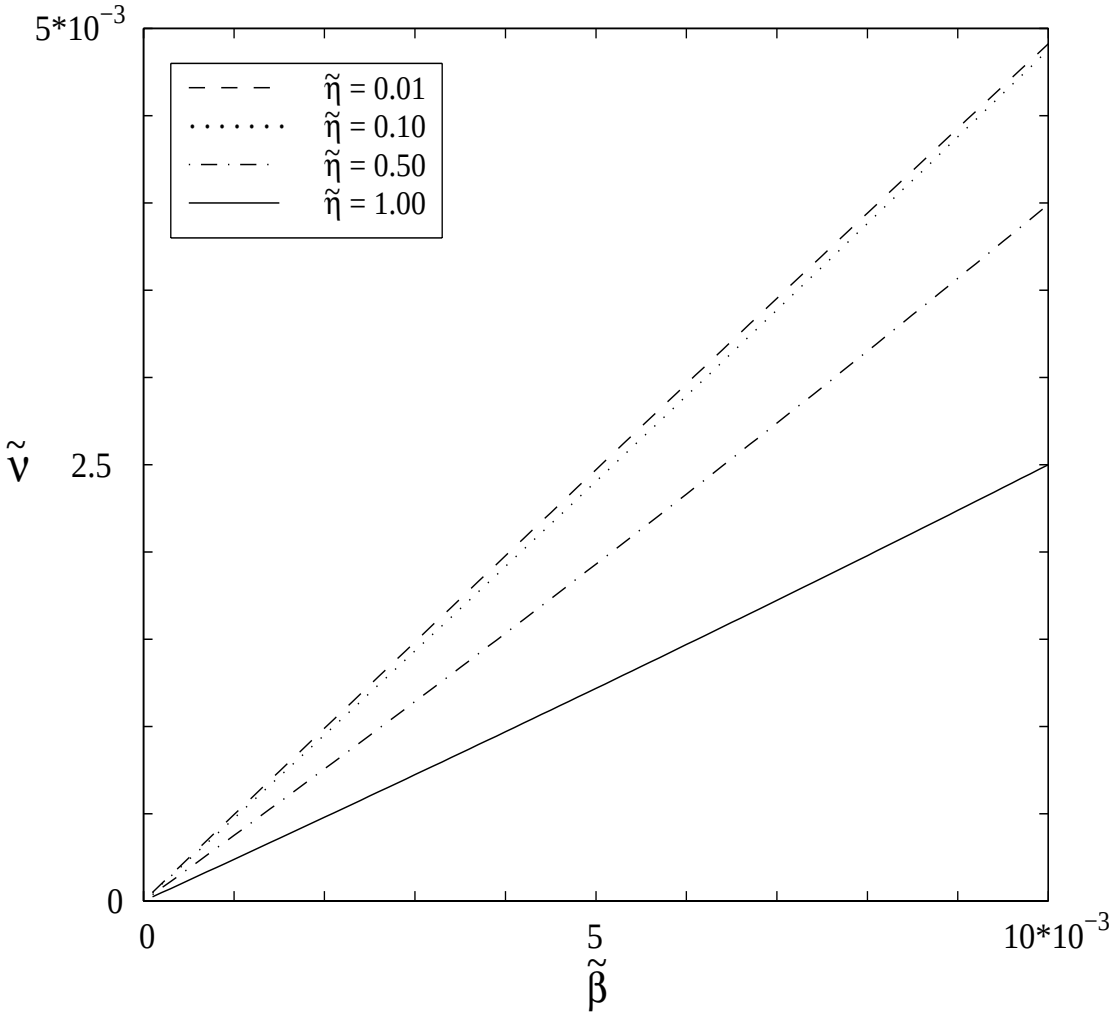

Figure 4.4: Lower hybrid oscillation damping rate $\tilde{\nu} = \nu/\omega_{\rm lh}$.

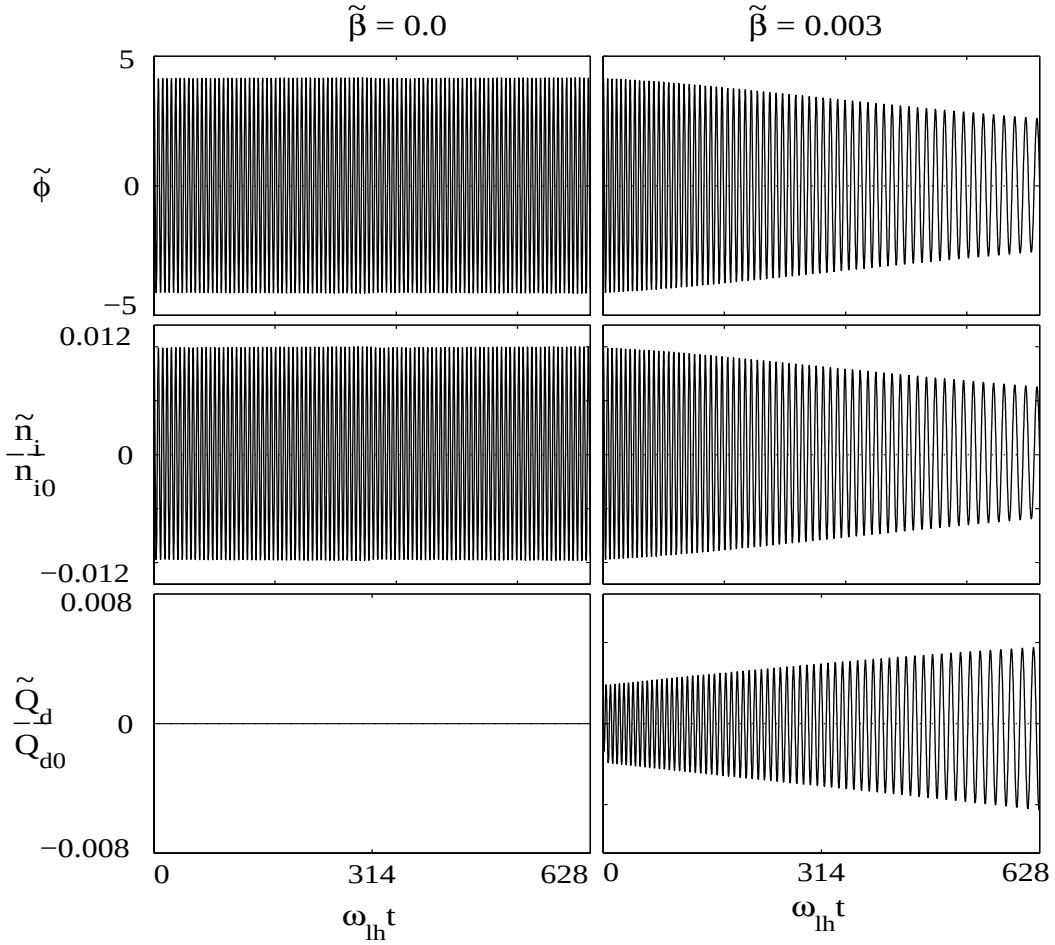

Figure 4.5: Temporal damping of lower hybrid oscillation potential and ion density and growth of dust charge fluctuations. $\tilde{\eta} = 1.0$.

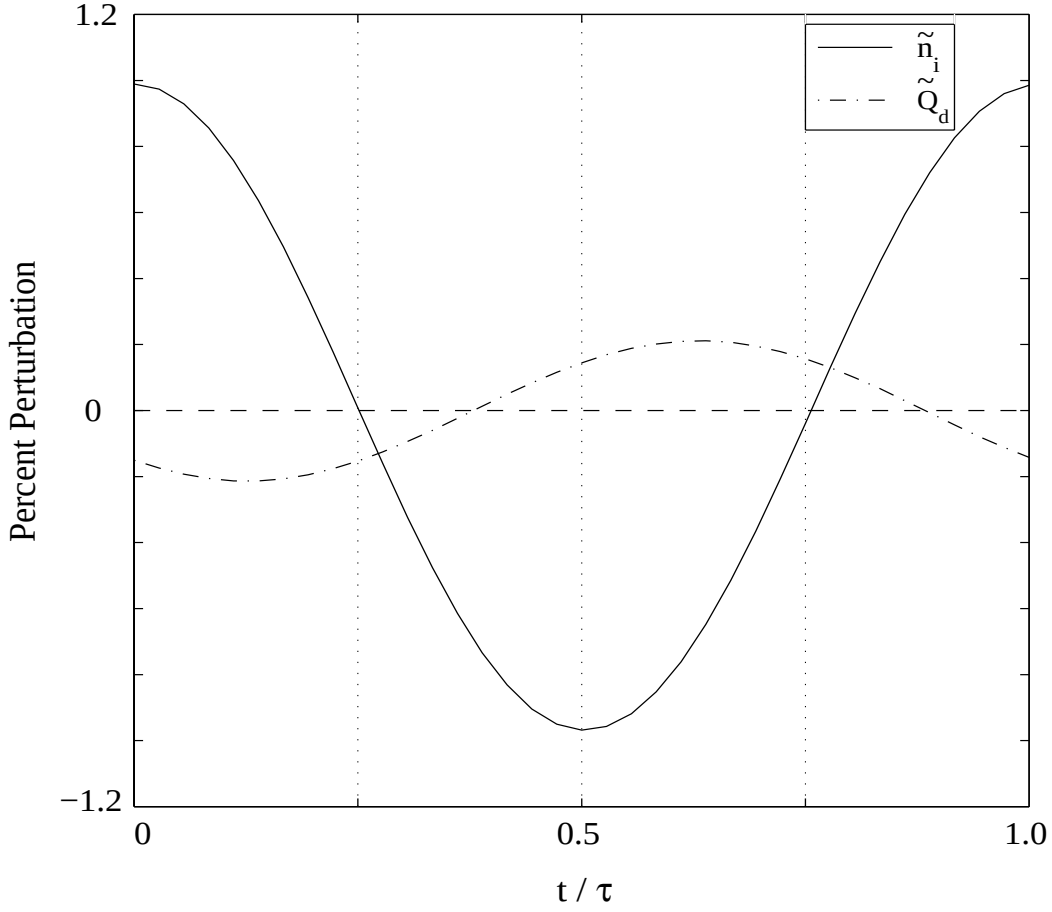

Figure 4.6: Plot showing temporal phase lag of dust charge relative to ion density for lower hybrid oscillations with $\tilde{\eta} = 1.0$ and $\tilde{\beta} = 0.003$.

$$\gamma \approx \frac{\sqrt{3}}{2^{1/3}} \omega_{\rm lh} \left(\frac{\omega_{\rm pd}}{\omega_{\rm pi}} \right)^{\frac{2}{3}}, \tag{4.13}$$

where $\omega_{\rm lh} \approx k v_{\rm d}$ (for maximum growth of waves).

4.3.2 Results

Figure 4.7 shows a numerical calculation of (4.12) for the beam strength parameter $\omega_{\rm pd}^2/\omega_{\rm pi}^2 = 0.01$. At maximum growth, the frequency, growth rate and wavelength scale as $\omega_{\rm r} \sim \omega_{\rm lh}$, $\gamma \sim \omega_{\rm lh}(\omega_{\rm pd}/\omega_{\rm pi})^{2/3}$, $\lambda \sim \ v_{\rm d}/f_{\rm lh}$, respectively. Inclusion of dust charge fluctuation effects is expected to introduce damping into the growth rate shown in Figure 4.7. This damping will be of the order of β as described in the previous section. However, for the weak beam limit, we find that the inclusion of dust charge fluctuations has minor effects on the linear wave growth. This can be seen by considering equation (4.9). For weak beams, typically, the parameter $n_{\rm d0}/n_{\rm e0}$ is expected to be quite small which implies β and therefore the damping is small. However, even though the linear development of the LHS instability is essentially unaffected by the dust charge fluctuations in this regime, we observe unique dust charging effects during the nonlinear development of the instability with our numerical model which we would like to discuss presently.

In our numerical simulation investigation, we consider the case of a weak beam with the classical beam strength parameter $\omega_{\rm pd}^2/\omega_{\rm pi}^2 = 0.01$. In this case, $n_{\rm d0} = 100$ dust particles per cell, $Q_{\rm d0} = 1000$ electrons and the dust charge is 1% of the background ion charge density. The dust streaming velocity is taken to be $10 v_{\rm ti}$. The dust charge fluctuation parameter $\tilde{\beta} = 0.002$. Figure 4.8 shows the time evolution of the electrostatic field energy and average floating potential $< e\phi_{\rm f} > /kT_{\rm e}$ for the simulation. Note that $< e\phi_{\rm f} > /kT_{\rm e}$ can be interpreted as the average negative charge on the dust particles. The field energy increases exponentially in the linear regime. The growth rate is in

good agreement with the theoretical value. The field energy oscillates after the LHS instability nonlinearly saturates. This oscillation is due to classical trapping [*Chen*, 1998]. The floating potential also oscillates as the dust grains collect and loose charge as they bounce in the potential wells. In the linear regime, the floating potential remains near the equilibrium value ($< e\phi_{\rm f0} > /kT_{\rm e} \approx 2.5$ for an equal temperature electron-hydrogen plasma [*Goertz*, 1989]). It should be noted that for the ratio $\frac{Q_{\rm d}}{m_{\rm d}}\frac{q_{\rm i}}{m_{\rm i}} \sim 10^{-3}$ as in this investigation, dust trapping dominates the ion trapping and the ion fluid approximation is valid. For smaller values of this ratio, ion trapping becomes more important and the fluid approximation for ions used here is no longer valid in the nonlinear regime. Figure 4.9 shows the density fluctuations of each species. Note that well defined perturbations in the dust charge as well as plasma ans dust densities are produced by the instability. Linear growth occurs to time $\omega_{\rm lh}t = 100$. The growth agrees well with equation (4.13) for the parameters under investigation. At later time nonlinear processes occur.

Associated with cold beam streaming instabilities is the modification of the velocity distribution function. This may be observed in the background plasma and/or beam plasma. The modification of the velocity distribution is one means of saturating the instability [*Winske and Rosenberg*, 1998; *Winske et al.*, 1995] and an important consequence of the nonlinear development of the instabilities in general. Modification in the velocity distribution of dust grains is observed in the simulations. We also observe an interesting new effect due to the incorporation of dust charge fluctuations. Considering a phase space of dust charge, we also observe nonlinear evolution of charges on the dust grains. Figure 4.10 shows the evolution of the phase space simultaneously for dust velocity and charge. These are shown at three different times during the simulation. At early times ($\omega_{\rm lh}t = 40$), the LHS instability can be seen to grow in both the dust velocity and charge by producing a small amplitude sinusoidal perturbation.

Later ($\omega_{\rm lh}t = 50$) some of the dust grains start to become trapped in the growing potential of the instability. Finally at late times ($\omega_{\rm lh}t = 100$), the charge phase space shows considerable scattering as well as the velocity phase space. Therefore nonlinear effects are seen to have fundamental effects on the dust charge. The charging and discharging of the dust particles as they bounce in the wave potential wells ultimately results in a broadening of the dust charge distribution in a manner similar to that of the broadening of the velocity distribution.

4.4 Plasma Instability Associated with Expanding Dust Clouds

4.4.1 Theory

Expansion of dust into a background plasma across a magnetic field has many applications in space plasmas [*Bernhardt et al.*, 1995; *Goertz*, 1989]. There are numerious physical processes associated with expansion of dust into a background plasma. Here we only consider the details of development of plasma instabilities. One likely source for the free energy required to drive plasma waves during the expansion of dust across a magnetic field into a background plasma is the inhomogeneity in the boundary between the the background plasma and dusty plasma produced by the dust charging. Steep boundary layer electron density gradients may be produced by electron capturing agents such as dust. Such a configuration may lead to highly sheared electron $\mathbf{E} \times \mathbf{B}$ flows in the boundary [*Ganguli et al.*, 1988]. If these electron flows have shear scale lengths of the order of or less than the ion gyroradius and shear frequencies of the order of the lower hybrid frequency, the EIH instability may result [*Ganguli et al.*, 1988; *Scales et al.*, 1995]. The EIH instability results in shear driven waves in the lower hybrid frequency range. Equation (4.7) may be used to calculate the dispersion relation of the EIH instability assuming a local approximation. The direction of the dust expansion is taken to be $\hat{\mathbf{x}}$ which implies the direction of the sheared $\mathbf{E} \times \mathbf{B}$ flow

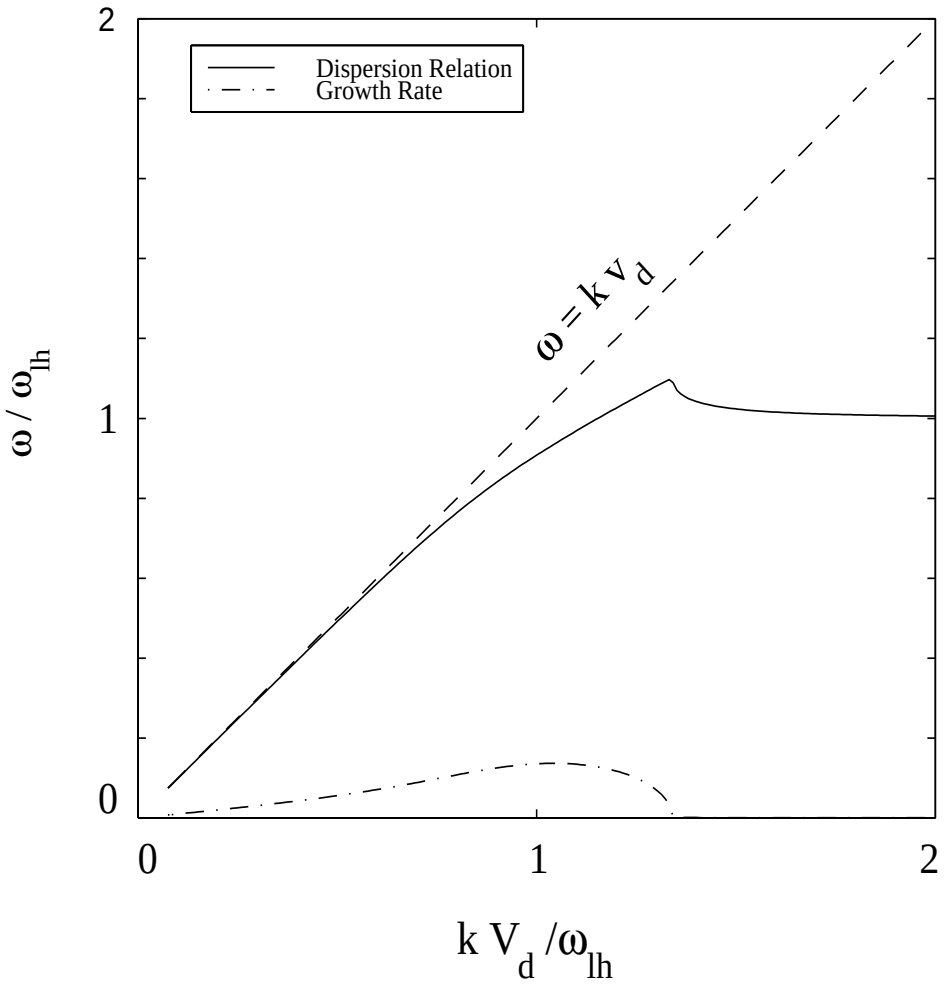

Figure 4.7: LHS instability dispersion relation and growth rate.

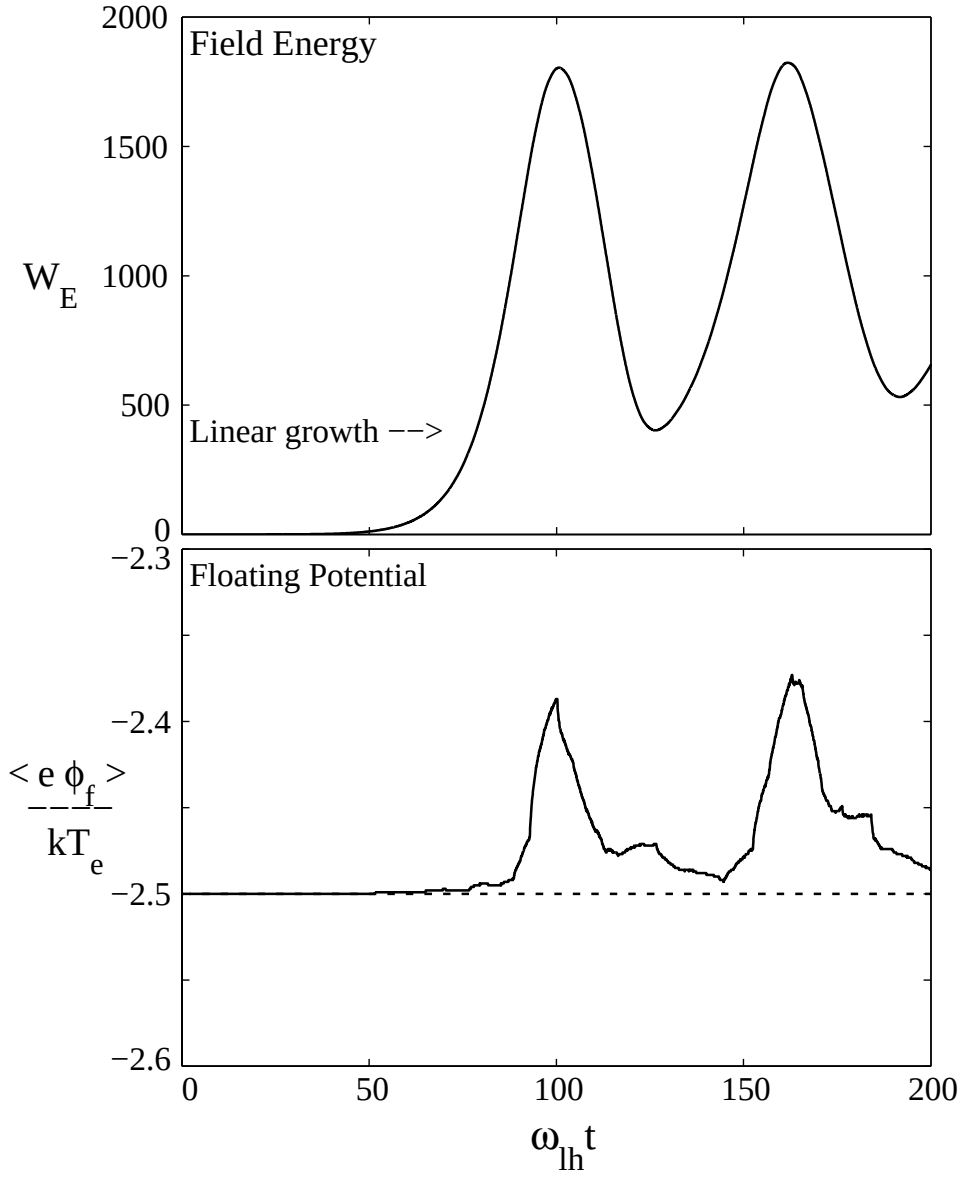

Figure 4.8: Time history of electric field energy and average floating potential for the LHS instability.

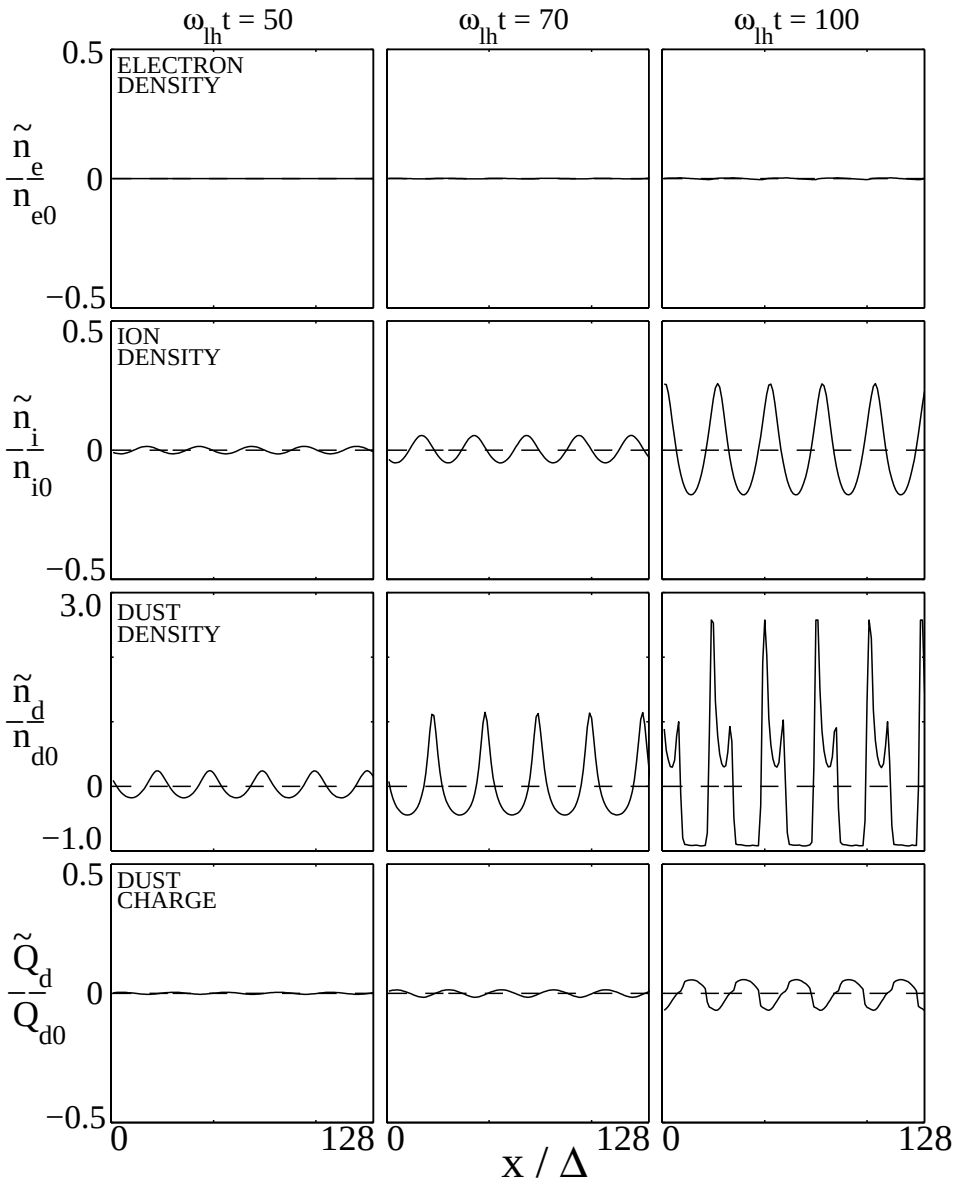

Figure 4.9: Electron, ion, and dust densities and dust charge for the LHS instability.

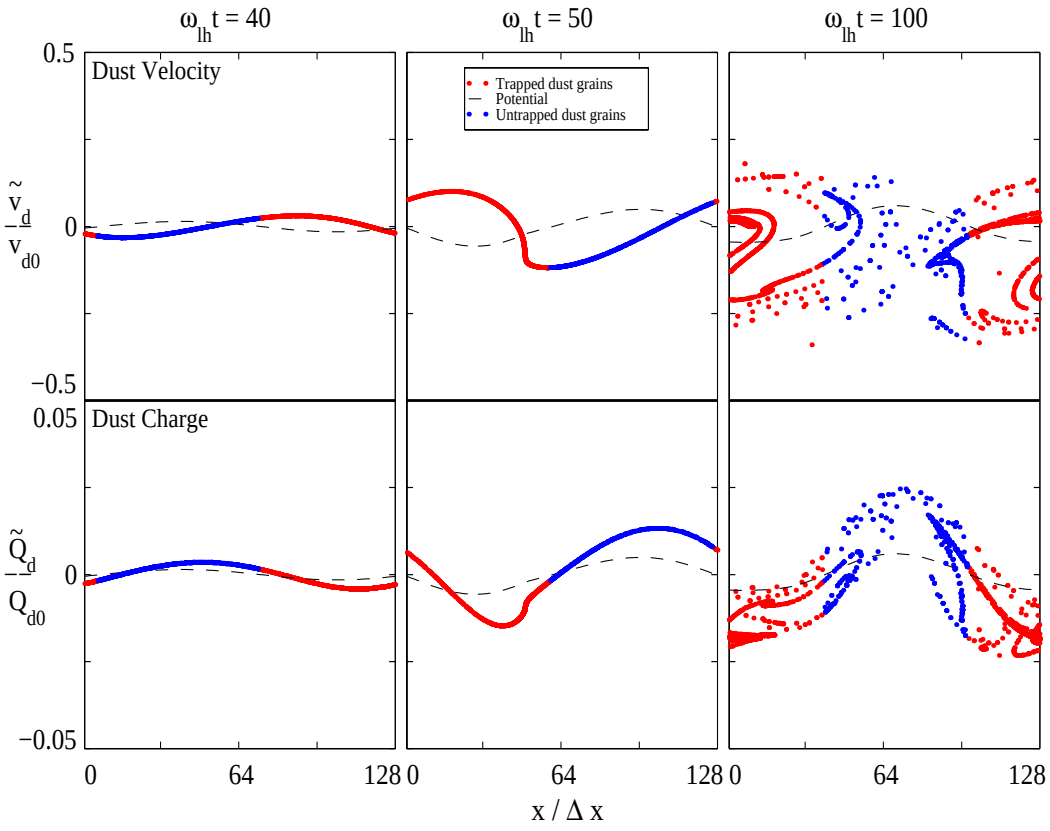

Figure 4.10: Numerical simulation results showing the development of the LHS instability. Note charge phase space as well as velocity phase space modification produced by the nonlinear evolution of the instability.

is $\hat{\mathbf{y}}$. From previous work [*Scales et al.*, 1995], we can write $\chi_{\rm i} = -\omega_{\rm pi}/\omega^2$ as before and $\chi_{\rm e} = -\omega_{\rm pi}^2/(\Omega_{\rm ci}(\omega - k_{\rm y}V_E)k_{\rm y}L_{\rm n})$ where V_E is the electron $\mathbf{E}\times\mathbf{B}$ flow velocity and $L_{\rm n} = (dn_{\rm e0}/dx)/n_{\rm e0}$ is the electron density gradient scale length. The dust motion may be neglected for simplicity and $\chi_{\rm d} = 0$. Using these susceptibilities, the local dispersion relation of this instability including the effects of dust charge fluctuations can be shown to be

$$\tilde{\omega}^4 + \left(\frac{\delta_{\rm i}S}{\tilde{k}_{\rm y}} - \frac{\alpha_{\rm i}}{\delta_{\rm i}}\tilde{k}_{\rm y} + i\tilde{\eta}\right)\tilde{\omega}^3 + \left(-1 + i\left(-\frac{\alpha_{\rm i}}{\delta_{\rm i}}\tilde{k}_{\rm y}\tilde{\eta} + \left(\tilde{\eta}+\tilde{\beta}\right)\frac{\delta_{\rm i}S}{\tilde{k}_{\rm y}}\right)\right)\tilde{\omega}^2 + \left(\frac{\alpha_{\rm i}}{\delta_{\rm i}}\tilde{k}_{\rm y} - i\left(\tilde{\eta} + \tilde{\beta}\frac{n_{\rm e0}}{n_{\rm i0}}\right)\right)\tilde{\omega} + i\left(\tilde{\eta} + \tilde{\beta}\frac{n_{\rm e0}}{n_{\rm i0}}\right)\frac{\alpha_{\rm i}}{\delta_{\rm i}}\tilde{k}_{\rm y} = 0 \tag{4.14}$$

where $\tilde{\omega} = \omega/\omega_{\rm lh}$, $\tilde{k}_{\rm y} = k_{\rm y}L_{\rm E}$, $\delta_{\rm i} = \omega_{\rm pi}/\Omega_{\rm ci}$, $S = L_{\rm E}/L_{\rm n}$, $\alpha_{\rm i} = V_{\rm E}/\Omega_{\rm ci}L_{\rm E}$, $L_{\rm E}$ is the electron flow velocity shear scalelength, $V_{\rm E}$ is the electron flow velocity, and $\Omega_{\rm ci}$ is the ion cyclotron frequency. Figure 4.11 and figure 4.12 shows numerical calculations of equation (4.14). The effect of increasing β is to reduce the growth rate and frequency slightly and narrow the bandwidth of the growing waves. The parameters are $\delta_{\rm i} = 24$, $S = 0.75$, $\alpha_{\rm i} = 244$, $L_{\rm E} = 6$, $V_{\rm E} = 11$, $L_{\rm n} = 8$, and $\Omega_{\rm ci} = 0.0075$. These parameters in simulation units correspond to the results to follow. The frequency, growth rate, and wavelength at maximum growth scale as $\omega_{\rm r} \sim \omega_{\rm lh}$, $\omega_{\rm i} \sim \omega_{\rm lh}$, $\lambda \sim L_{\rm E}$. In the results presented in figure 4.11 and figure 4.12, we have taken $\tilde{\eta}$ and $\tilde{\beta} = 0$ for simplicity. Figure 4.13 shows a reduction of the growth rate with increasing β and decreasing η.

4.4.2 Results

Figure 4.14 and figure 4.15 show the electron and ion densities and dust charge for $\tilde{\beta} = 0.15$ and $\tilde{\beta} = 0.7$ for the EIH instability. These figures clearly show that the dust

charge decreases with time as the plasma depletion can be observed to develop. Figure 4.16 shows electron flow velocities at $\tilde{\beta} = 0.15$ and $\tilde{\beta} = 0.7$.

In the numerical simulation results to be presented, the dust is allowed to diffusively expand across the magnetic field into the background plasma at a speed of approximately $0.3v_{\rm ti}$ in the $\hat{\mathbf{x}}$ direction. The dust is taken to have an equilibrium charge $Q_{\rm d0}$ of 300 electrons and 100 dust grains per cell are used. The dust charge density is $0.75n_{\rm i0}$. Therefore, the dust charge is larger than the initial electron charge density unlike the previous two cases discussed.

As the dust expands across the magnetic field, the charging of the dust and reduction of electron density produces and sustains a well-defined boundary layer between the dusty plasma and the background plama. An ambipolar electric field develops across the boundary ($\hat{\mathbf{x}}$ direction) which produces a highly sheared electron $\mathbf{E} \times \mathbf{B}$ flow velocity along the boundary ($\hat{\mathbf{y}}$ direction). These are the conditions necessary for the development of the EIH instability. Figure 4.17 and Figure 4.18 show the time evolution of the electric field energy for $\tilde{\beta} = 0.15$ and $\tilde{\beta} = 0.7$ during the simulation. The energy in the ambipolar field $E_{\rm x}$ can be seen to grow initially as the dust expands and charges. The $\mathbf{E} \times \mathbf{B}$ electron flow resulting from this field is highly sheared and provides free energy for development of lower hybrid waves propagating in the $\hat{\mathbf{y}}$ direction. Subsequently, the $E_{\rm y}$ field grows due to the development of the EIH instability. This velocity shear-driven instability produces vortex-like structures of wavelength of the order of the velocity shear scale size. Figure 4.19 and figure 4.20 shows the two dimensional electron and ion density as well as the dust charge at the end of the simulation ($\omega_{\rm pi}t = 12.6$) for the previous Figure. For the parameter regime under consideration, the dust motion may be neglected so the dust density is not shown. Mode 4 has been chosen to be excited in the simulations. The simulation has a relatively large value of $\tilde{\beta} \cong 0.7$. Well defined vortex structures are observed to develop in the dust charge $Q_{\rm d}$ as well as the electron density. The development of the vortices in the nonlinear evolution of the EIH instability broadens the boundary layer and reduces the flow velocity and velocity

shear. This ultimately saturates the growth of the instability as can be seen in Figure 4.17 in the field energy. Well defined vortices in the dust charge are due to the fact that the charge fluctuations are able to follow the electron and ion density fluctuations faithfully. This is because the relatively large value of $\tilde{\beta}$ indicates a rapid development of the dust fluctuations in response to the electron density perturbations as described in section 4.2. Smaller values of $\tilde{\beta}$ show negligible dust charge fluctuations produced by the EIH instability. The results indicate the importance of wave perturbations in the dust charge as well as the electron and ion densities. The growth rate and frequency observed in the simulations generally agrees well with the theoretical predictions from (4.14).

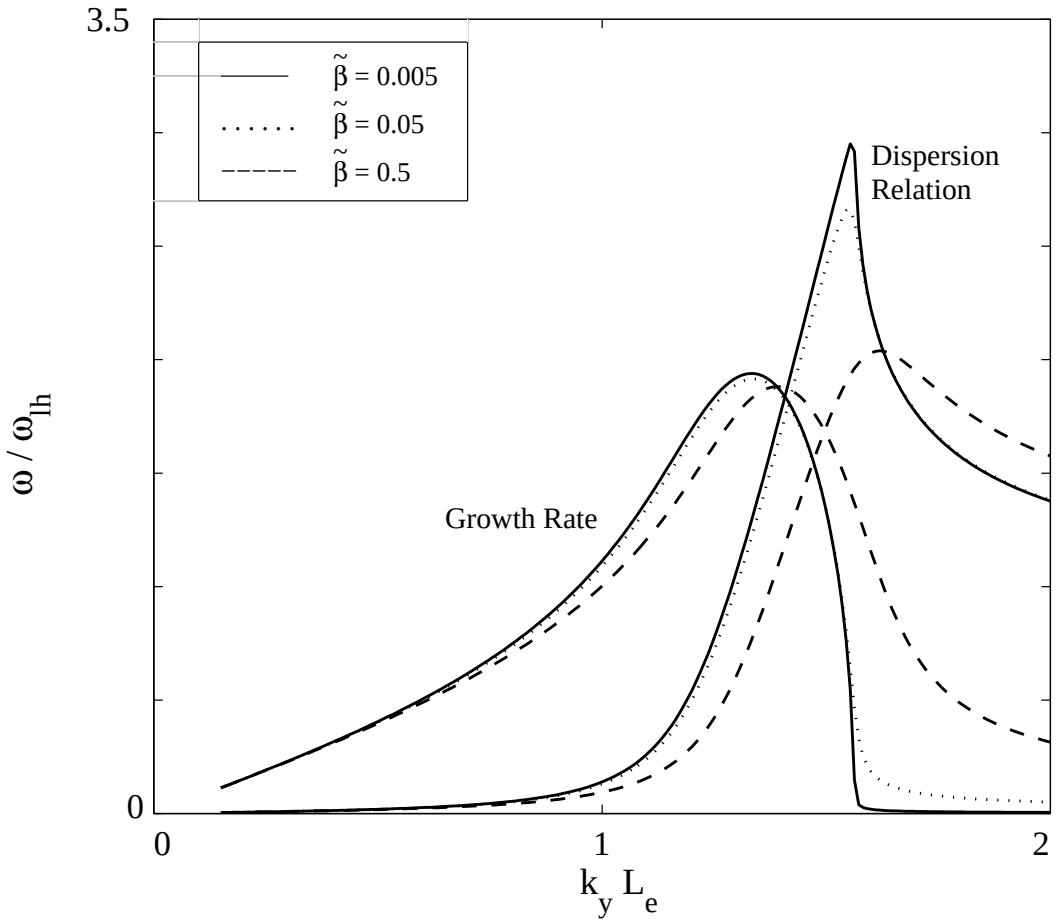

Figure 4.11: EIH instability dispersion relation and growth rate *vs* wavenumber.

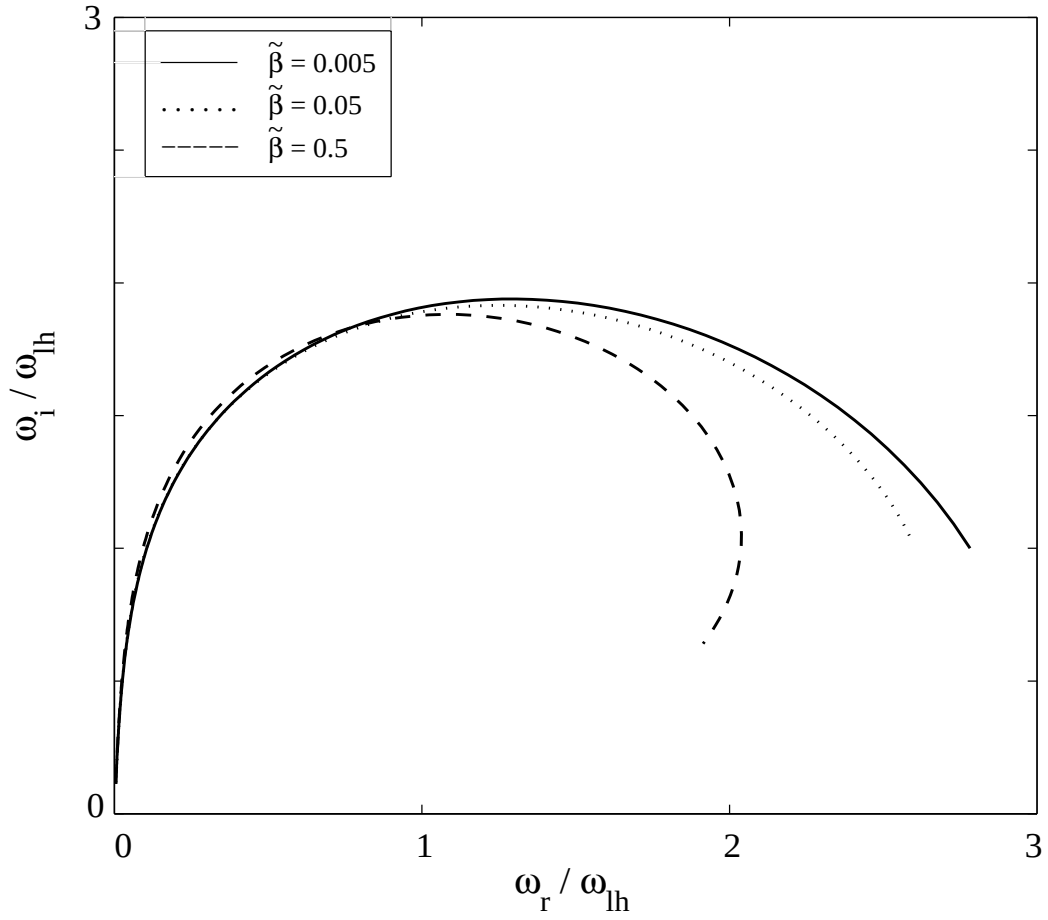

Figure 4.12: EIH instability growth rate *vs* frequency.

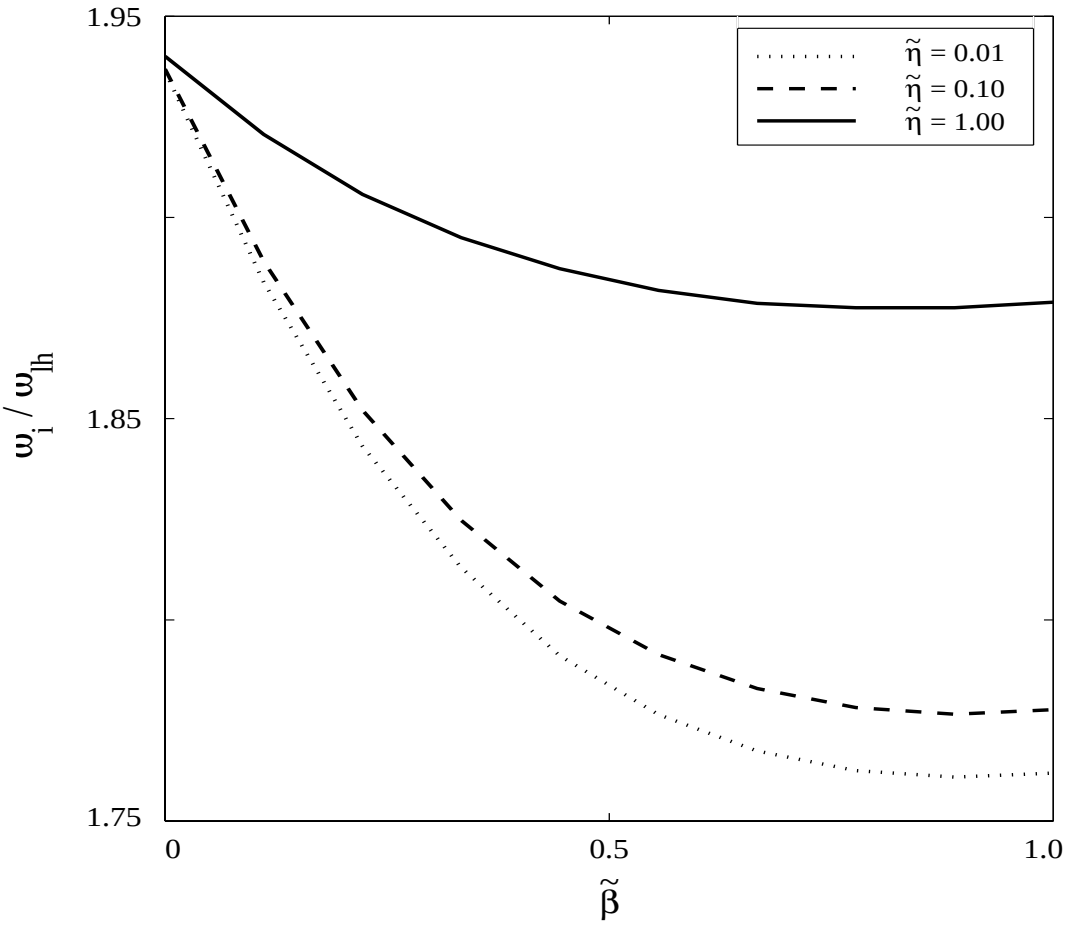

Figure 4.13: EIH instability growth rate *vs* $\tilde{\beta}$ for $\tilde{\eta} = 0.01$, 0.1, and 1.0.

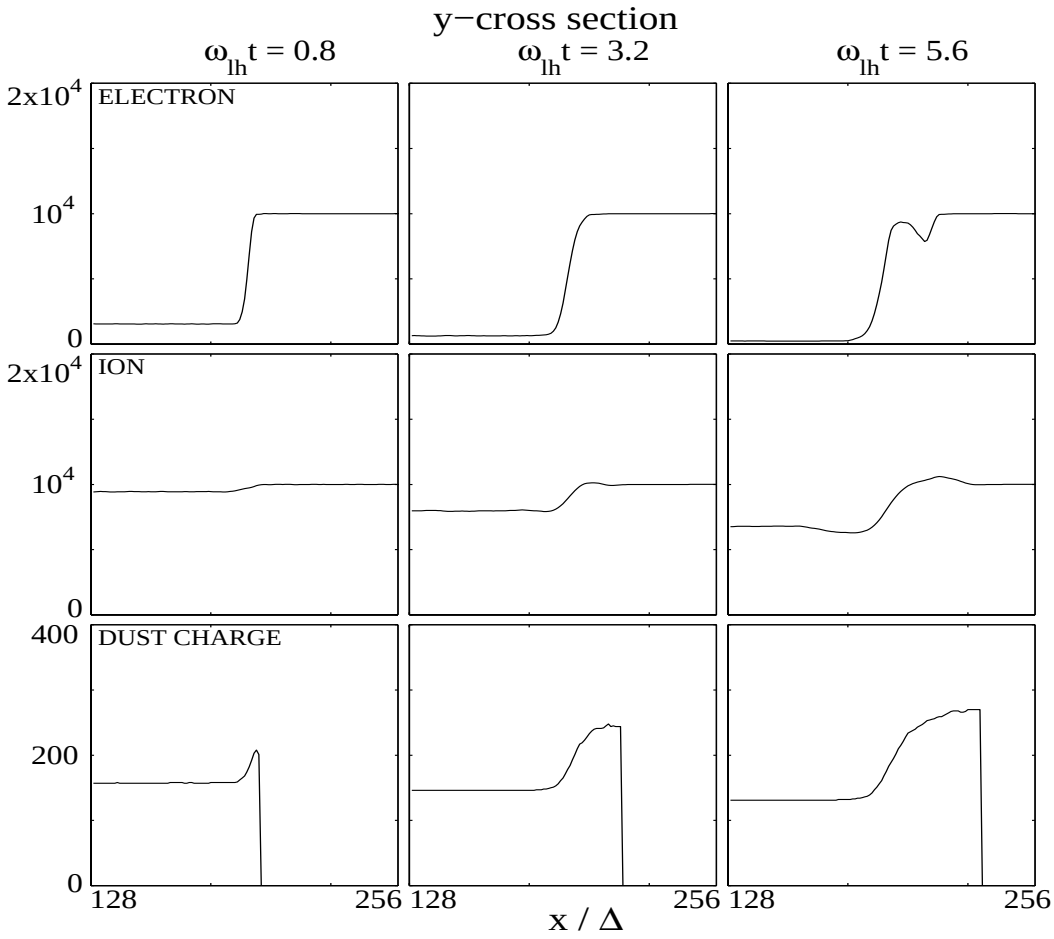

Figure 4.14: Electron and ion densities and dust charge at $\tilde{\beta} = 0.15$ for EIH instability.

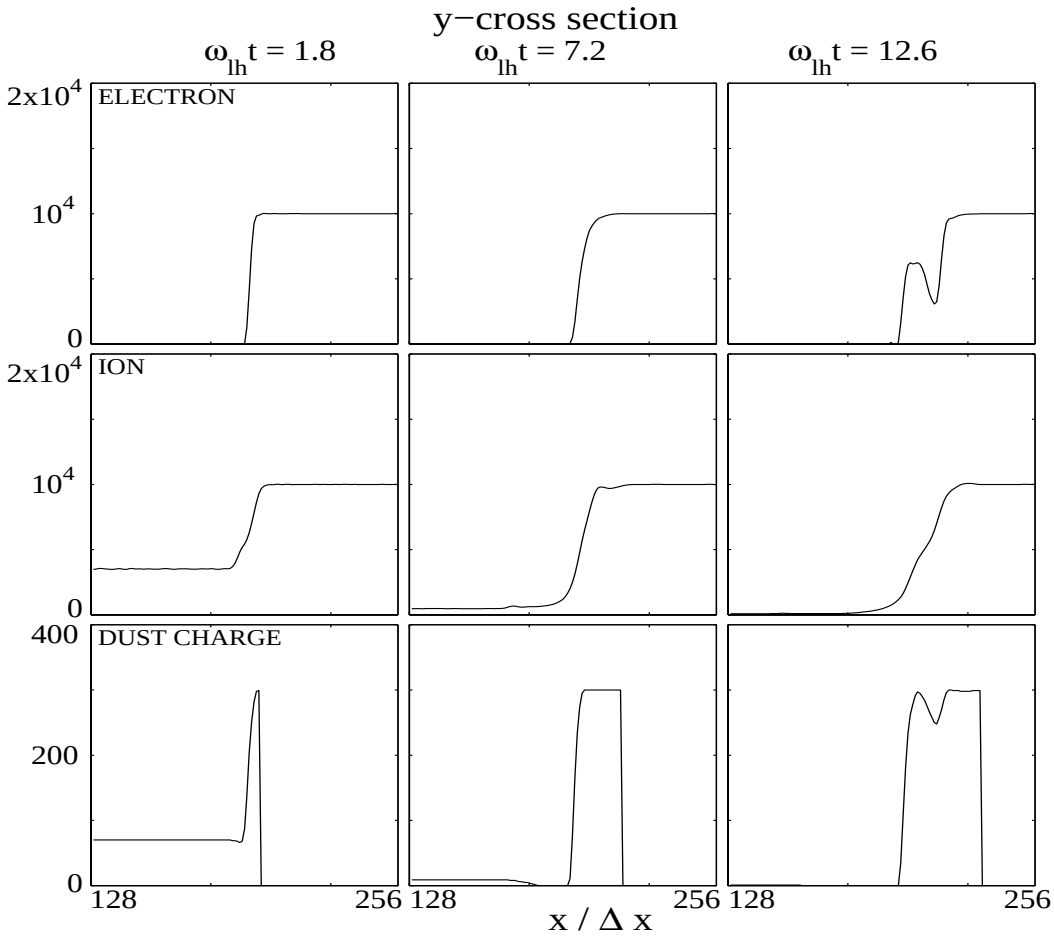

Figure 4.15: Electron and ion densities and dust charge at $\tilde{\beta} = 0.7$ for EIH instability.

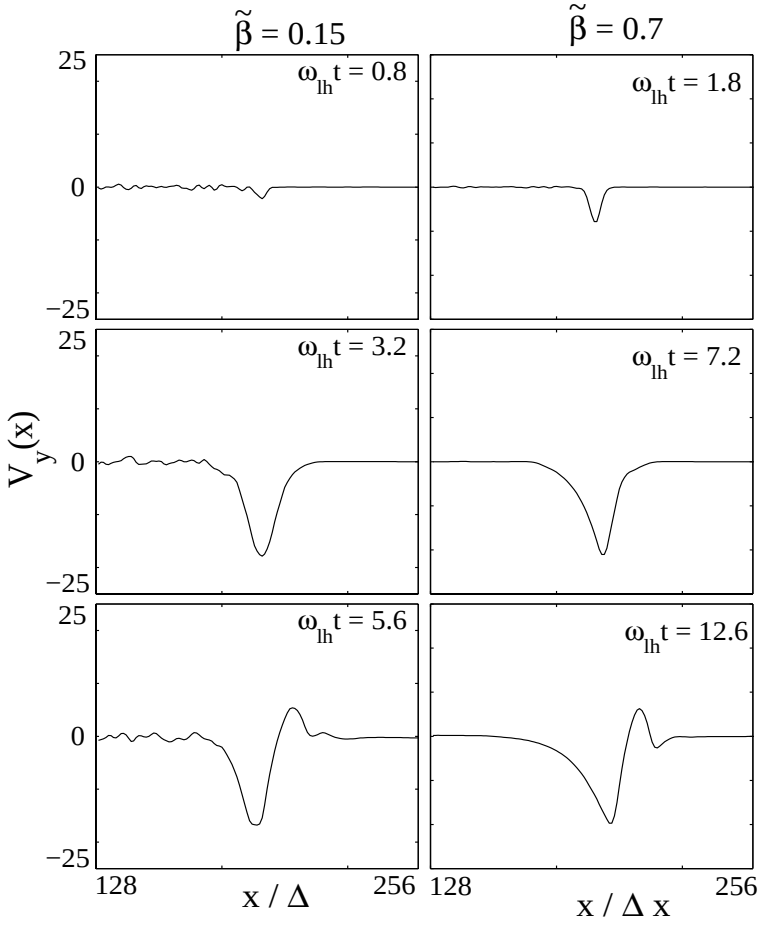

Figure 4.16: Electron flow velocities at $\tilde{\beta} = 0.15$ and $\tilde{\beta} = 0.7$ for EIH instability.

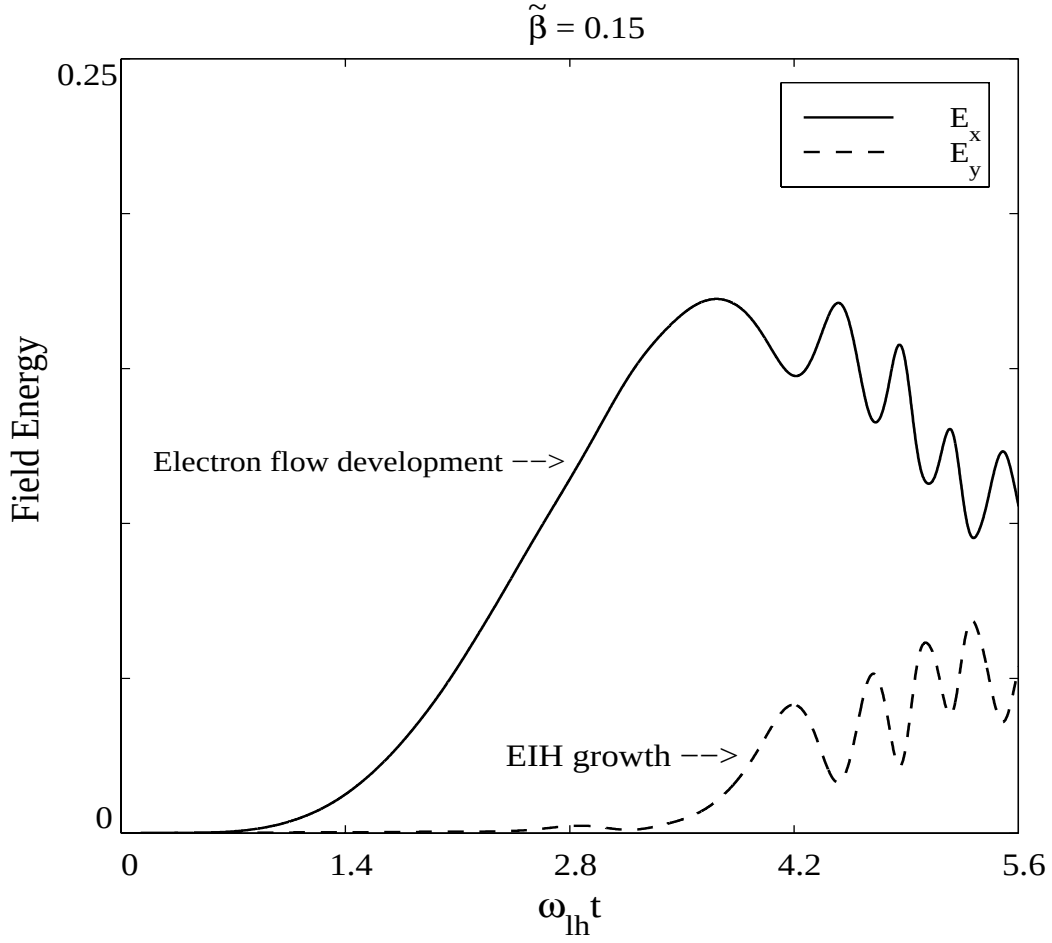

Figure 4.17: Time evolution of EIH instability electrostatic field energy at $\tilde{\beta} = 0.15$.

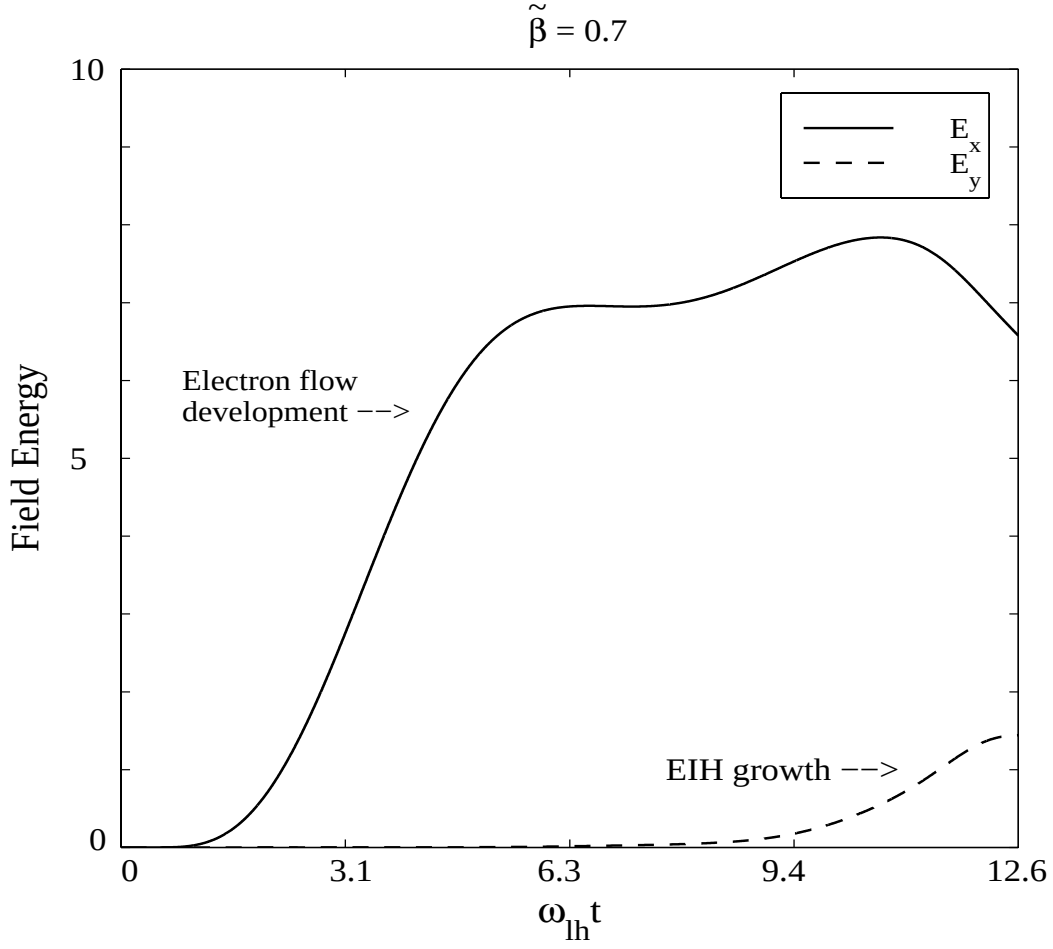

Figure 4.18: Time evolution of EIH instability electrostatic field energy at $\tilde{\beta} = 0.7$.

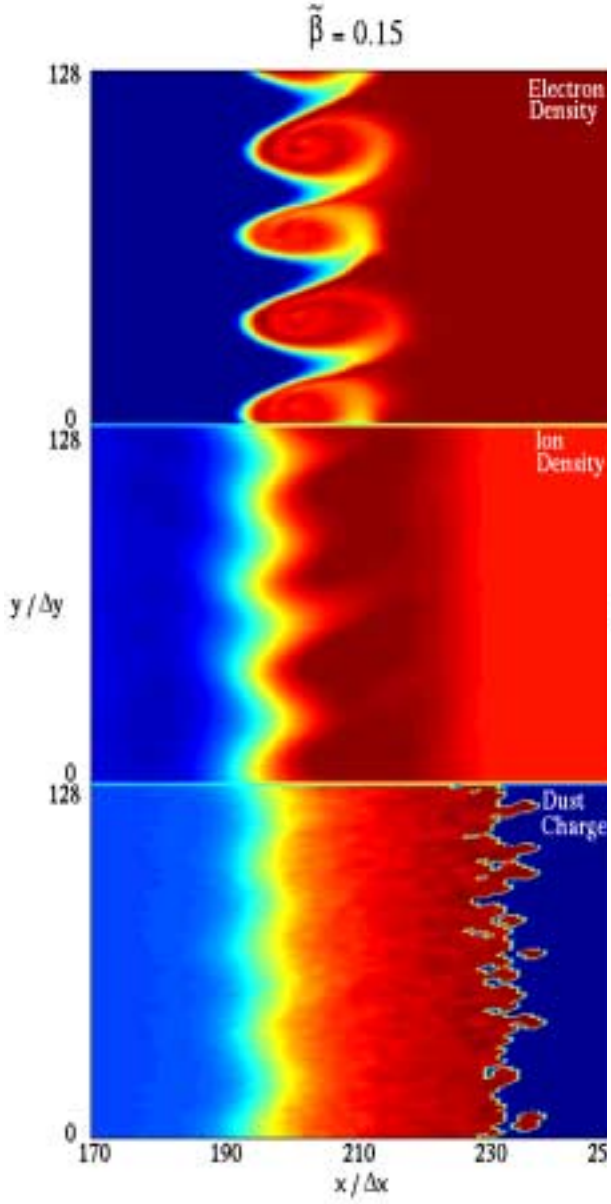

Figure 4.19: EIH instability 2-D plasma density and dust charge for $\omega_{\rm lh}t = 12.6$ at $\tilde{\beta} = 0.15$.

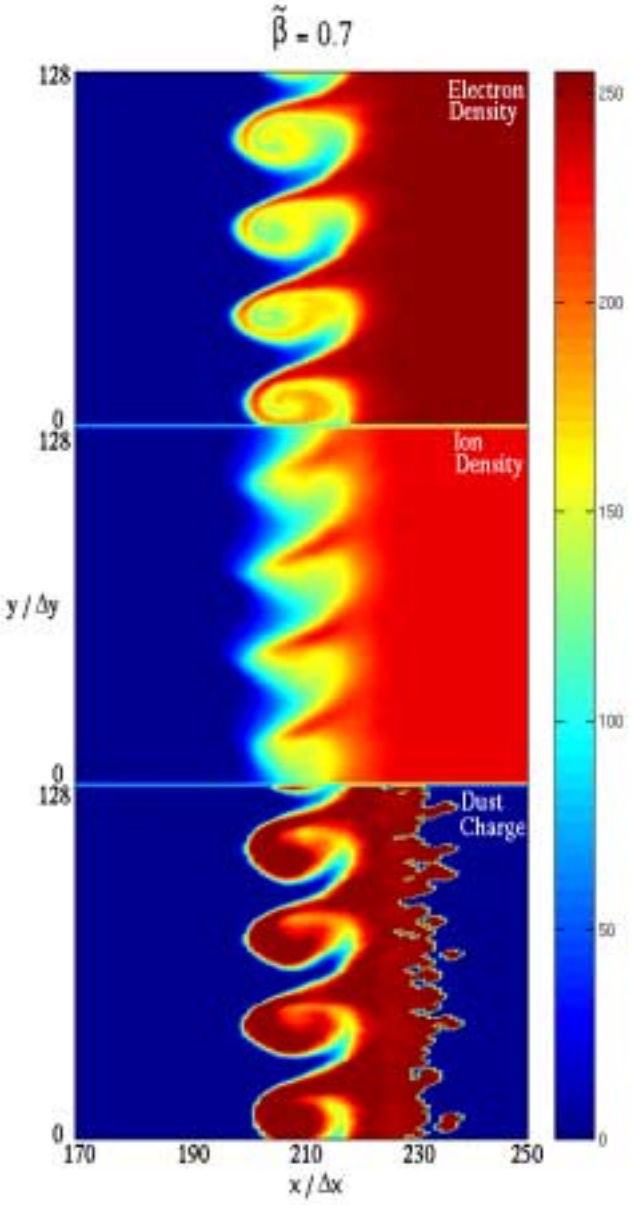

Figure 4.20: EIH instability 2-D plasma density and dust charge for $\omega_{\rm lh}t = 12.6$ at $\tilde{\beta} = 0.7$.